A new dataset of rain cells based on observations of Tropical Rainfall Measuring Mission (TRMM) precipitation radar, visible/infrared scanner and microwave imager

Zhenhao Wu[1], Jian Shang[2], Chunguan Cui[3], Peng Zhang[2], Songyan Gu[2], and Lin Chen[2], Yunfei Fu[1]

[1]School of Earth and Space Sciences, CMA-USTC Laboratory of Fengyun Remote Sensing, University of Science and Technology of China, Hefei, 230026, China

[2]Key Laboratory of Radiometric Calibration and Validation for Environmental Satellites, National Satellite Meteorological Center, China Meteorological Administration, Beijing, 100081, China

[3]Institute of Heavy Rain, China Meteorological Administration, Wuhan, 430205, China

Correspondence: Yunfei Fu (fyf@ustc.edu.cn)

Abstract. Understanding the characteristics of rain cell, the most basic unit in natural precipitation system, is helpful to improve the cognition of the precipitation system. In this study, based on the merged data of precipitation profile data, reflectivity and infrared data, and microwave brightness temperature data, which were observed by the Tropical Rainfall Measuring Mission (TRMM) precipitation radar (PR), visible and infrared scanner (VIRS) and TRMM microwave imager (TMI), rain cells were identified in the PR swath by two methods, the minimum bounding rectangle (MBR) method and the best fit ellipse (BFE) method. The geometric and physical parameters of rain cell were also defined. By analyzing the geometric parameters (length, width, height and so on) and physical parameters (rain rate, visible reflectivity and thermal infrared brightness temperature from cloud top, and microwave brightness temperature from cloud column) of two rain cells (weak rain cell and strong rain cell) identified by MBR method and BFE method, results indicate that the strong rain cell is filled with deep convective precipitation and also has low thermal infrared bright temperature in cloud top, while the weak rain cell is stratiform precipitation with small rain rate. Compared to the BFE method, the MBR method has a smaller rain cell length, while both methods demonstrate similar rain cell widths. The filling ratio of BFE method is slightly higher than that of MBR method. In general, the both methods indicate that the rain cell identification and the defined rain cell parameters are reasonable and intuitive. The data which were used in this paper are freely available at https://doi.org/10.5281/zenodo.13118878 (Wu and Fu, 2024).

1 Introduction

Precipitation is an important part of the global energy and water cycle (Houze, 1997; Oki and Kanae, 2006; Lau and Wu, 2010). In the water cycle, the rain cell that constitutes a precipitation system can be considered the most elementary unit in different definitions. The investigation of the three-dimensional structure of rain cell is helpful to understand the thermodynamic structure and microphysical processes within precipitation systems (Houze, 1981; Zipser and Lutz, 1994; Yuter and Houze, 1995; Fu and Liu, 2001). Austin and Houze (1972) found subsynoptic scale precipitation regions that each had rather clearly definable characteristics and behavior when they studied the precipitation patterns in New England. Based on radar observations and rain gauge records, they also divided precipitation pattern into synoptic areas, large mesoscale areas, small mesoscale areas and cells. The rain cell with area of about 10 km^2 in radar echo was regarded as a single cumulus convective unit in their study (Gagin et al., 1986; Capsoni et al., 1987).

More studies were done by defining the threshold of rain cell, such as an area where rain rates were greater than a given threshold (Goldhirsh and Musiani, 1986). For example, Capsoni et al. (1987) defined rain cell as the connected region with rain rate greater than 5 $mm\ h^{-1}$ based on S-band radar observation near Milan in 1980. Awaka (1989) modified rain rate threshold to 0.4 $mm\ h^{-1}$. Meanwhile, many studies exposed the relationship between rain rate threshold and rain cell size based on ground-based radar data (Konrad, 1978; Sauvageot et al., 1999; Feral et al., 2000; Begum and Otung, 2009). Feral et al. (2000) adopted elliptic fitting method to investigate the geometric characteristics and directional distribution of rain cell. The statistical results also revealed that the major axis length was twice longer than the minor axis length and the direction distribution was uniform in the majority of the rain cells.

Since the late 1990s, observations of precipitation radar (PR), visible and infrared scanner (VIRS) and TRMM microwave imager (TMI) aboard the TRMM satellite provided a wealth of data for systematical study cloud and precipitation (Kummerow et al., 1998, 2000; Nesbitt et al., 2000; Viltard et al., 2000; Liu and Fu, 2001; He et al., 2006; Schumacher and Houze, 2003; Li and Fu, 2005; Liu and Fu, 2010; Fu, 2014). With the massive data observed by PR, VIRS and TMI, Nesbitt et al. (2006), Liu et al (2007, 2008), and Liu and Zipser (2013) made spick-and-span studies in the field of rain cell identification and its parameters with elliptic fitting method. Their rain cell data were also widely used on analyzing the temporal and spatial distribution characteristics of rain cell (Zhou et al., 2013; Yokoyama et al., 2014; Ni

et al., 2015), such as that line shaped convective systems occurred more frequently over ocean, and showed higher frequency in the subtropics (Liu and Zipser, 2013). To continue reveal the characteristics of rain cell parameters, Fu et al. (2020) defined the geometric and physical parameters of rain cell, used the minimum bounding rectangle (MBR) method to identify the rain cell within the width of the PR scan, calculated these parameters and obtained their characteristics. The data of rain cell generated from MBR method was applied to study the morphological characteristics of rain cell in summer Tibetan Plateau (Chen et al., 2021). Cai et al. (2024) adopted the three methods, minimum circumscribed ellipse, minimum bounding rectangle and direct indexing area, for rain cell fitting. They also compared the geometric characteristics generated from the three methods.

However, the rain cell data identified by MBR method need to add reflectivity and infrared temperature observed by VIRS and microwave bright temperature measured by TMI, which will give full play to the advantages of TRMM instruments. For the above purposes, our study merged observation data of PR, VIRS and TMI at PR pixel resolution, then used two methods, the minimum bounding rectangle (MBR) method and the best fit ellipse (BFE) method, to identify rain cell and produce a new dataset with precipitation parameter, visible/infrared and microwave signal. The structure of this study is as follows: section 2 describes data and data merging methods, section 3 introduces rain cell identification method, section 4 defines the geometric and physical parameters of rain cell, section 5 analyzes two typical rain cells in geometric and physical parameters. Access to the datasets is introduced in section 6, and conclusions are presented in section 7.

2 Data

The TRMM was jointly developed by the US National Aeronautics and Space Administration (NASA) and the Japan Aerospace Exploration Agency (JAXA) and launched on November 27, 1997. The TRMM is a non-solar synchronous polar-orbiting satellite with an orbital inclination of 35° and observes a location between 38° S and 38° N (Simpson et al., 1996; Kummerow et al., 1998, 2000). The satellite carries five instruments: PR, VIRS, TMI, the Lighting Imaging Sensor (LIS), the Cloud and Earth Radiant Energy Sensor (CERES). This study mainly involves the measurements of TRMM PR, VIRS, and TMI.

2.1 PR data 2A25

The PR was the first spaceborne precipitation radar onboard the TRMM. It is a single-frequency microwave radar with a frequency of 13.8 GHz (Kummerow et al., 1998; Kozu et al., 2001). PR scans in the cross-track direction with a scanning inclination of 17°. There are 49 pixels on each scanning line. The horizontal resolution is about 4.3 km at nadir (5.0 km after the orbital boost), and the scanning width is 215 km (245 km after the orbital boost). It can detect the three-dimensional structure of precipitation from mean sea level to 20 km (a total of 80 layers) with a vertical resolution of 0.25 km.

The 2A25 data is the second-level data product of the TRMM PR, which is generated by inverting the echo signals detected by the PR. This dataset mainly includes scanning time, geographic information, three-dimensional rain rate, rain type and so on (Awaka et al., 1997). The detection sensitivity of the PR is about 17 dBZ, corresponding to the rain rate of about 0.4 $\mathrm{mm\ h^{-1}}$ (Schumacher and Houze, 2003). Therefore, when the rain rate of the pixels is lower than 0.4 $\mathrm{mm\ h^{-1}}$, the default value is set and will not be involved in the calculation.

2.2 VIRS data 1B01

The VIRS scans in the cross-track direction with a scanning angle of 45°. There are 261 pixels on each scanning line. The scanning width is 720 km (833 km after the orbital boost), and the horizontal resolution is 2.2 km at nadir (2.4 km after the orbital boost). It has five channels from visible to the far infrared band: CH1 (0.63 μm), CH2 (1.6 μm), CH3 (3.7 μm), CH4 (10.8 μm) and CH5 (12.0 μm). The 1B01 is a first-level data product of VIRS, which includes the reflectivity at CH1 and CH2, the infrared radiation brightness temperature at CH3, CH4, and CH5 after the correction and calibration of the VIRS detection results.

2.3 TMI data 1B11

The TMI is a nine-channel passive microwave radiometer with five frequencies spanning from 10 to 85 GHz. The microwave signal frequencies are 10.65 GHz, 19.35 GHz, 21.3 GHz, 37.0 GHz, and 85.5 GHz, except for 21.3 GHz, which is a single vertical polarization channel. The other four frequencies are horizontal (H) and vertical (V) polarization dual channels. The scanning width is 760 km (878 km after the orbital boost). The horizontal resolution of each frequency channel (effective field of view of beam, Kummerow et al., 1998) varies from 63 km × 37 km at 10.65 GHz to 7 km × 5 km at 85.5 GHz. The 1B11 data contains the calibrated TMI-detected microwave brightness temperature at multiple channels.

2.4 The merged data of 2A25, 1B01 and 1B11

To comprehensively analyze the parameters of precipitation, cloud top spectral signal and particle phase in precipitation system, the rain rate profile and echo profile of 2A25, the reflective and infrared temperature of 1B01, and the microwave brightness temperature of 1B11 were collocated in PR horizontal resolution and produced a merged data. The reason for that is because the difference spatial resolution of the three instruments, but the time lag of observation among the three instruments to the same target is less than 1min, i.e. the quasi-synchronous observations (Liu et al., 2008; Fu et al., 2011; Sun and Fu, 2021). Statistics showed about 7 VIRS pixels within 1 PR pixel. It was found that the spectral signals of VIRS changed weakly after merging, the mean change was less than 0.7 %, and the mean square deviation was less than 2.5 % (Fu et al., 2011). Due to TMI channels have different spatial resolutions that is larger than PR pixel resolution, the nearest neighbor method was used to obtain microwave brightness temperature at PR pixel resolution, i.e. each PR pixel was assigned the microwave brightness temperatures of nine channels a TMI pixel closest to the PR pixel (Liu et al., 2008).

3 The algorithm of rain cell identification

The definition of rain cell in this study is the same as that proposed by Fu et al. (2020), i.e. a rain cell consists of at least four connected rain pixels within the swath of PR scan. According to the working mode of PR, its swath consists of 49 pixels (from number 1 to 49), so if the identified rain cell has pixels at the edge of the PR swath (the first pixel and 49th pixel), the rain cell is not included. If the identified rain cell is at the beginning and end of the PR swath, the rain cell is also eliminated. The advantage of this is to avoid the truncation effect of PR swath. To automatically identify rain cell in the merged data, the best fit ellipse (BFE) method and the minimum bounding rectangle (MBR) method were used. The two methods can calculate an ellipse and a rectangle with the smallest area covering the target object (rain cell), respectively, as did by Nesbitt et al. (2006) and Fu et al. (2020). The slight differences of geometric parameters calculated by MBR method and BFE method show in the length and width of rain cell, while the physical parameters calculated by the both methods are the same. The rain cell parameters identified by the two methods presented in this study can be used by studies according to their own preferences.

4 The definitions of rain cell parameters

The definition of geometric and physical parameters describing the identified rain cell was almost the same as that of Fu et al. (2020). The specific geometric parameters were listed in Table 1, in which the first six parameters descript the horizontal geometry of rain cell and the rest do the vertical geometry. These parameters have a clear physical meaning, such as α represents the horizontal shape of rain cell, a small (large) α indicates that the horizontal shape of rain cell is more like a strip (square) precipitation system, and has more (less) correlation with a frontal precipitation system. The variable β expresses the ratio of rain cell area (S_{rain}) to the area of the MBR or BFE frame (S), and characterizes the effectiveness of both methods used to identify rain cell. Large (small) β indicates more (less) rain pixels inside the MBR or BFE frame. The variables γ_{max} and γ_{av} represent the three-dimensional spatial shape of rain cell. Small γ_{max} (γ_{av}) indicates a "squatty" appearance of rain cell, in contrast to a "lanky" appearance for large γ_{max} (γ_{av}).

Table 1. Geometric parameter definitions of rain cell by the minimum bounding rectangle (MBR) method and the best fit ellipse (BFE) method

Parameters in MBR method	Parameters in BFE method
L_r (km), length	L_e (km), length of the major axis
W_r (km), width	W_e (km), length of the minor axis
α_r, horizontal shape index, $\alpha_r = W_r/L_r$	α_e, horizontal shape index, $\alpha_e = W_e/L_e$
S_r (km^2), MBR area, $S_r = L_r * W_r$	S_e (km^2), BFE area, $S_e = \frac{\pi}{4} * L_e * W_e$
β_r, filling ratio, $\beta_r = S_{rain}/S_r$	β_e, filling ratio, $\beta_e = S_{rain}/S_e$
S_{rain} (km^2), rain area, sum of all rain pixel areas in rain cell	
H_{max} (km), maximum echo top height in rain cell	
H_{av} (km), mean echo top height in rain cell	
γ_{max}, maximum spatial morphology index of rain cell, $\gamma_{max} = H_{max}/L$	
γ_{av}, mean spatial morphology index of rain cell, $\gamma_{av} = 2H_{av}/(L+W)$	
H_{avc} (km), mean echo top height of convective precipitation in rain cell	
H_{avs} (km), mean echo top height of stratiform precipitation in rain cell	
H_dBZ_{max} (km), height of the maximum reflectivity factor in rain cell	
μ, ratio of the maximum reflectivity factor height to the maximum echo top height in rain cell	

The physical parameter definitions of rain cell by MBR method and BFE method were listed in Table 2 including rain type, rain rate profile, reflectivity factor profile, mean rain rate, visible reflectivity and infrared brightness temperature, microwave brightness temperature and so on. Those parameters are significant to represent the intensity, the inhomogeneity, and the evolution stage of rain cell.

Table 2. Physical parameter definitions of rain cell by the minimum bounding rectangle (MBR) method and the best fit ellipse (BFE) method.

Symbol	Physical meaning
RR_{ave} (mm h^{-1})	Mean rain rate in rain cell
RR_{max} (mm h^{-1})	Maximum rain rate in rain cell
RR_{avc} (mm h^{-1})	Mean convective rain rate in rain cell
RR_{avs} (mm h^{-1})	Mean stratiform rain rate in rain cell
RR_{maxc} (mm h^{-1})	Maximum rain rate of convective precipitation in rain cell
RR_{maxs} (mm h^{-1})	Maximum rain rate of stratiform precipitation in rain cell
CAF (%)	Convective area fraction to total precipitation area in rain cell
SAF (%)	Stratiform area fraction to total precipitation area in rain cell
CPC (%)	Convective precipitation contribution to total precipitation in rain cell
SPC (%)	Stratiform precipitation contribution to total precipitation in rain cell
dBZ_{max} (dBZ)	Maximum reflectivity factor in rain cell
RF_{ave}	Mean reflectivity of VIRS visible or near infrared channel in rain cell
RF_{avc}	Mean reflectivity of VIRS visible or near infrared channel for convective precipitation in rain cell
RF_{avs}	Mean reflectivity of VIRS visible or near infrared channel for stratiform precipitation in rain cell
TB_{ave} (K)	Mean brightness temperature of VIRS mid-infrared and far-infrared, TMI channel in rain cell
TB_{avc} (K)	Mean brightness temperature of VIRS mid-infrared and far-infrared, TMI channel for convective precipitation in rain cell
TB_{avs} (K)	Mean brightness temperature of VIRS mid-infrared and far-infrared, TMI channel for stratiform precipitation in rain cell

5 Results

5.1 Precipitation parameters of rain cell

In order to better understand the geometric and physical parameters of the defined rain cell identified by MBR method and BFE method, two rain cells were analyzed below. One identified rain cell A, occurred on 2 June, 1999 in southern Tibetan Plateau (TRMM orbit 08691), and the other, rain cell B, on 13 June, 2003 in eastern Tibetan Plateau (TRMM orbit 31787). Figure 1 shows the distribution of rain rate and rain type for the two rain cells, the frame of both MBR and BFE is also plotted, which clearly showed the length and width of MBR method, and the long and short axis of BFE method. Statistics of parameters for the two rain cells shows in Table 3. Figure 1a shows that rain cell A identified by MBR method has length 290.86 km (L_r), width 140.29 km (W_r), rain area 10223.5 km^2 (S_{rain}), MBR area 40803.36 km^2

(S_r), and filling ratio 0.25 (β_r). The horizontal shape index is 0.48 (α_r), which indicates rain cell A with a strip like shape. The rain cell A identified by BFE method (Figure 1c) has length 347.63 km (L_e), width 139.94 km (W_e), rain area 10223.5 km^2 (S_{rain}), BFE area 38207.27 km^2 (S_e), and filling ratio 0.27 (β_e). The horizontal shape index is 0.4 (α_e), which also indicates rain cell A with a strip like shape. The rain cell B identified by MBR method and BFE method showed in Figure 1b and 1d, its parameters listed in Table 3 show it slightly like strip shape.

The vertical parameters of the both rain cells identified by the both methods listed in Table 3 show no differences in method because statistics were made in rain pixels inside rain cell. Comparing rain cell A and B, the latter has higher echo top (H_{max} = 17.75 km, H_{av} = 9.47 km), and shows like "lanky" appearance (γ_{max} = 0.11, γ_{av} = 0.08). In rain cell B, the mean echo top height of convective precipitation and stratiform precipitation, 10.39 km and 7.96 km, is also higher than that in rain cell A, which indicates that the updraft velocity within rain cell B is strong and the precipitating cloud is deep. The ratio of the maximum reflectivity factor height to the maximum echo top height μ is 0.37 and 0.15 for rain cell A and B, respectively. Combining γ_{max} and μ it can be concluded that rain cell B is a deep precipitation system with large particles in the lower part of cloud.

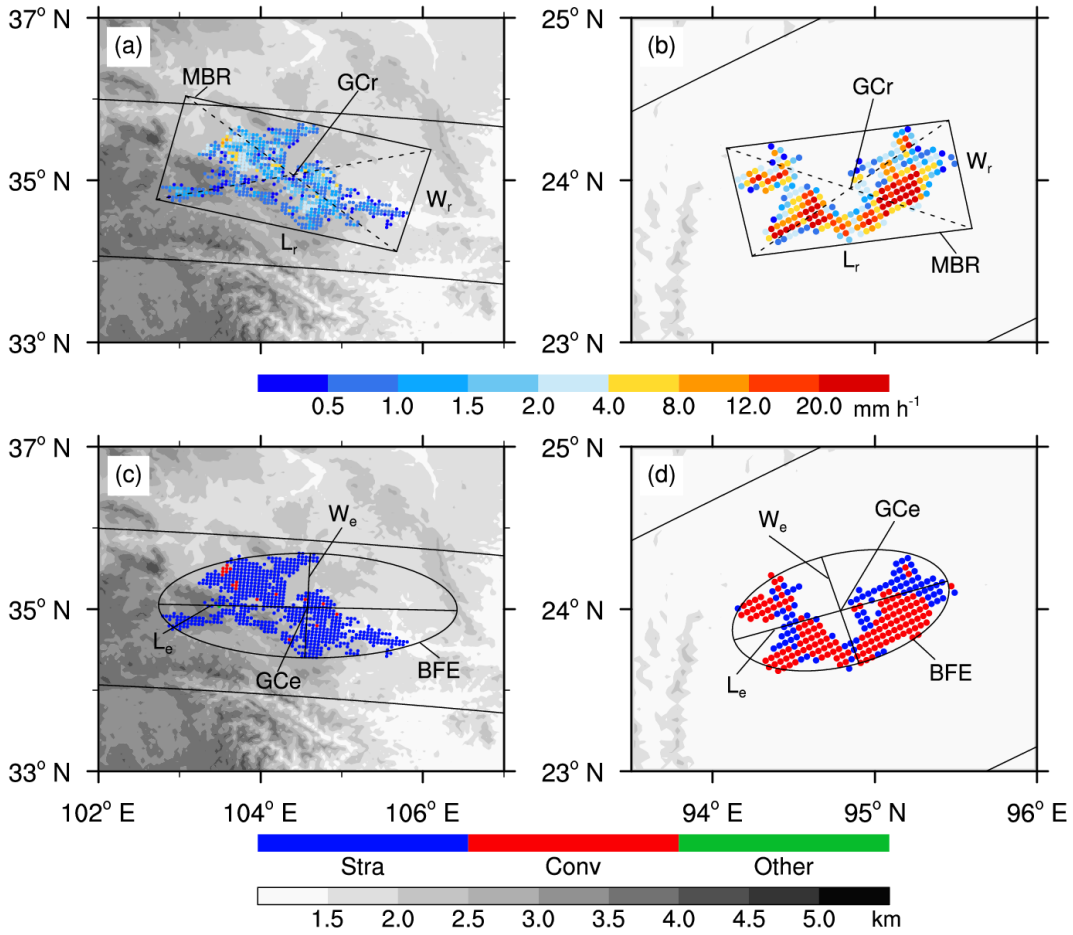

Figure 1. Two rain cells occurred on June 2, 1999 and June 13, 2003 measured by PR: rain rate (a and b) and rain type (c and d, blue, red and green represent for stratiform, convective and other precipitation, respectively). The two rain cells in up panel were identified by MBR method, in bottom by BFE method. GCr and GCe represent for geometric center of rain cell identified by MBR method and BFE method, respectively. The gray level in the figure represents the elevation of the terrain.

The physical parameters of the both rain cells identified by the both methods were listed in Table 4. PR observation showed that the mean rain rate RR_{ave} and the maximum rain rate RR_{max} of rain cell B were 11.64 mm h^{-1} and 113.14 mm h^{-1}, respectively, and rain cell A was a relatively weak rain cell. The defined physical parameters also showed that the mean convective rain rate is 5.52 mm h^{-1} and 17.35 mm h^{-1}, the mean stratiform rain rate 1.16 mm h^{-1} and 2.31 mm h^{-1}, for rain cell A and B, respectively. The defined CAF (convective area fraction to total precipitation area) and SAF (Stratiform area fraction to total precipitation area) are 2.56 %/62.01 % and 97.3 %/37.99 % in rain cell A/B, while CPC (convective precipitation contribution to total precipitation) and SPC (stratiform precipitation contribution to total precipitation) are 11.14 %/92.46 % and 88.79 %/7.54 % in rain cell A/B. This indicates that rain cell B is a convective cell while rain cell A is a stratiform rain cell. Actually, the rain

cell B has the maximum reflectivity factor 57.81 dBZ (dBZ_{max}) listed in Table 4 against 36.38 dBZ for rain cell A.

Table 3. The geometric parameters of rain cell A and B calculated by MBR method and BFE method.

MBR method		BFE method	
L_r (km)	290.86/169.57	L_e (km)	347.63/170.66
W_r (km)	140.29/76.18	W_e (km)	139.94/76.76
α_r	0.48/0.45	α_e	0.4/0.45
S_{rain} (km^2)	10223.50/4496.40	S_{rain} (km^2)	10223.50/4496.40
S_r (km^2)	40803.36/12917.48	S_e (km^2)	38207.27/10289.43
β_r	0.25/0.35	β_e	0.27/0.44
H_{max}(km)	8.75/17.75		8.75/17.75
H_{av} (km)	5.59/9.47		5.59/9.47
γ_{max}	0.03/0.11		0.03/0.11
γ_{av}	0.03/0.08		0.03/0.08
H_{avc} (km)	5.76/10.39		5.76/10.39
H_{avs} (km)	5.58/7.96		5.58/7.96
H_dBZ_{max} (km)	3.25/2.75		3.25/2.75
μ	0.37/0.15		0.37/0.15

Table 4. The physical parameters of rain cell A and B calculated by MBR method and BFE method.

Physical parameter			
RR_{ave} (mm h^{-1})	1.27/11.64	$RF1_{ave}$	0.72/0.69
RR_{max} (mm h^{-1})	8.08/113.14	$RF1_{avc}$	0.73/0.66
RR_{avc} (mm h^{-1})	5.52/17.35	$RF1_{avs}$	0.72/0.73
RR_{avs} (mm h^{-1})	1.16/2.31	$TB_{10.8\_ave}$ (K)	253.65/222.96
RR_{maxc} (mm h^{-1})	8.08/113.14	$TB_{10.8\_avc}$ (K)	252.42/221.51
RR_{maxs} (mm h^{-1})	4.45/11.87	$TB_{10.8\_avs}$ (K)	253.68/225.31
CAF (%)	2.56/62.01	$TB_{19GHz\_H\_ave}$ (K)	260.61/276.75
SAF (%)	97.3/37.99	$TB_{19GHz\_H\_avc}$ (K)	258.38/275.79
CPC (%)	11.14/92.46	$TB_{19GHz\_H\_avs}$ (K)	260.66/278.32
SPC (%)	88.79/7.54	$TB_{85GHz\_H\_ave}$ (K)	254.44/219.11
dBZ_{max} (dBZ)	36.38/57.81	$TB_{85GHz\_H\_avc}$ (K)	252.84/212.72
		$TB_{85GHz\_H\_avs}$ (K)	254.49/229.53

5.2 VIRS and TMI signals of rain cell

Since TRMM PR, VIRS and TMI observed the same target in spatiotemporal synchronization, the spatial distribution of visible reflectivity (0.63 μm) and far-infrared brightness temperature (10.8 μm) for the two rain cells can be given as shown in Figure 2. The figure also shows the rain cell area identified by MBR method and BFE method, which indicates many strips of reflectivity (larger than 0.8) and uniform

distribution of brightness temperature (varying from 240 to 250 K) for rain cell A, while rain cell B consists of two convective clouds with reflectivity greater than 0.85 and brightness temperature lower than 220 K. Table 4 also shows the calculated mean visible reflectivity $RF1_{ave}$ for the two rain cells (0.72 and 0.69, respectively). The mean visible reflectivity of convective/stratiform precipitation $RF1_{avc}/RF1_{avs}$ for the two rain cells are 0.73/0.72 and 0.66/0.73, respectively. The large reflectivity values indicate that the cloud optical thickness at the top of the two rain cells are large. The mean brightness temperature at VIRS channel 10.8 μm ($TB_{10.8\_ave}$) shows 253.65 K and 222.96 K for the two rain cells, which indicates that rain cell B has a higher cloud top, i.e. ice phase distributed at cloud top. While the cloud top of rain cell A has ice-liquid mixed phase. The signals of VIRS channels can be used to retrieval cloud parameters. The retrieval algorithms were studied and reviewed by many authors (Nakajima and King, 1990; Rossow and Garder, 1993; Han et al., 1994; Rossow and Schiffer, 1999; Fu, 2014).

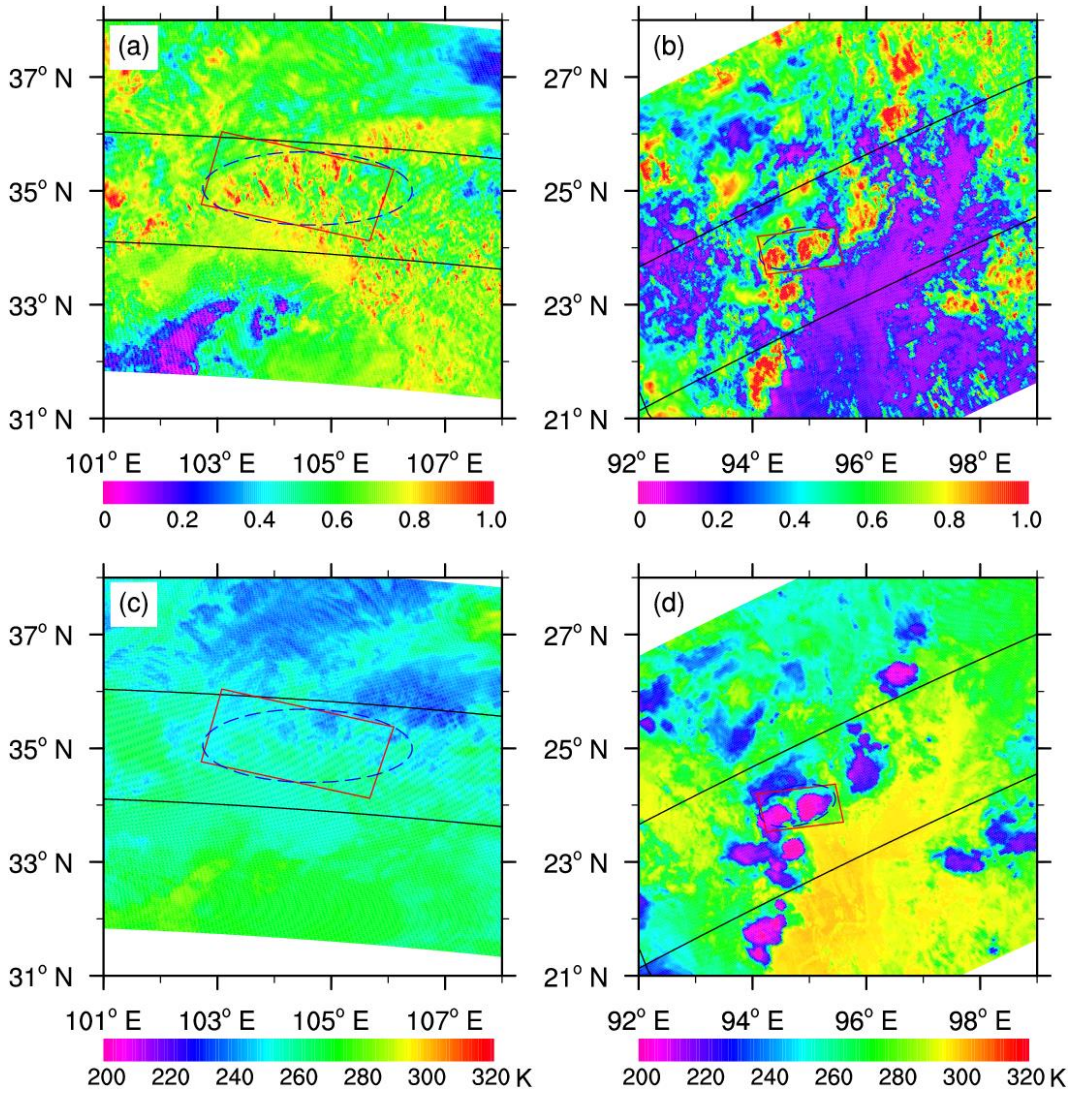

Figure 2. The reflectivity distribution of visible channel at 0.63 μm (a and b) and brightness temperature distribution of far-infrared channel at 10.8 μm (c and d) for the two cases observed by VIRS (Visible and Infrared Scanner). The solid black line is PR (Precipitation Radar) scanning track. The red solid rectangle and blue dash ellipse represent for the area of rain cell identified by MBR method and BFE method, respectively.

Similar to Figure 2, the distribution of microwave brightness temperature observed by nine channels of TMI can be given. But for simplicity, Figure 3 only plotted the distribution of brightness temperature at TMI horizontal polarization channel 19.4 GHz and 85 GHz. At channel 19.4 GHz, rain cell A shows relatively lower brightness temperature (from 250 to 280 K), rain cell B has higher brightness temperature (from 260 to 290 K). Because the low-frequency microwave channel is easily affected by the radiation on land surface, it can be judged that the temperature of land surface in rain cell A is lower than that in rain cell B. The brightness temperature of microwave high frequency channels is mainly affected by the composition of ice phase inside cloud, such as ice particles and supercooled water, while the influence of land surface radiation on these channels is weak. The more content of ice phase composition inside cloud, the lower brightness temperature at these high frequency channels. According to this principle, rain cell B shows low brightness temperature at 85 GHz in Figure 3d because the rain cell belongs to deep convective precipitation system. While rain cell A has more stratiform precipitation and less ice particles, so the brightness temperature at this same channel is higher. In Table 4, the mean brightness temperature at channel 19.4 GHz and 85 GHz also indicates the difference between the two rain cells, and the difference between the two rain types. The microwave brightness temperature of TMI channels can be used to retrieval cloud parameters such as ice water or liquid water or rain rate based on retrieval algorithms of previous studies (Grody, 1976; Grody et al., 1980; Liu and Curry, 1993; Petty, 1994a, 1994b; Wang et al., 2009; Fu, 2021).

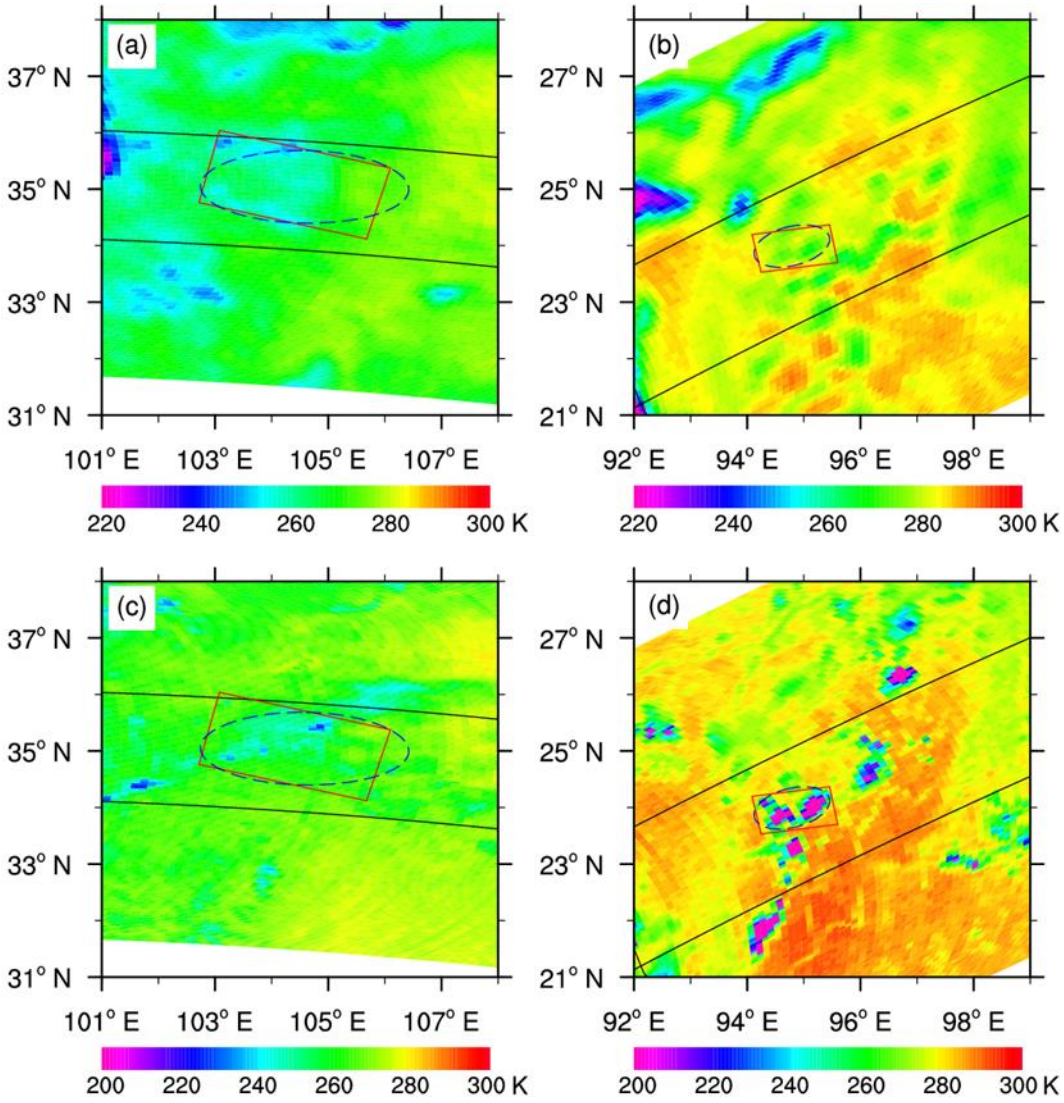

Figure 3. The brightness temperature distribution of microwave horizontal polarization channel at 19 GHz (a and b) and at 85 GHz (c and d) for the two cases observed by TMI (TRMM Microwave Imager). The solid black line is PR (Precipitation Radar) scanning track. The red solid rectangle and blue dash ellipse represent for the area of rain cell identified by MBR method and BFE method, respectively.

In order to visually display the parameter distribution of rain cell A and B identified by MBR method and BFE method, Figure 4 shows the distribution of rain rate, reflectivity at VIRS visible channel, brightness temperature at VIRS thermal infrared channel, microwave brightness temperature at TMI low frequency and high frequency channel. It must be pointed out that both VIRS and TMI signals in Figure 4 correspond to PR precipitation pixels (that is, signals corresponding to each resolution of PR pixel), and these signals are not given if there is no precipitation area in the rain cell. Therefore, the rain cell data established in this study facilitate the study of relationship among precipitation, visible/infrared and microwave signals.

A simple application is shown in Figure 5, which displays the multi-parameter distribution along the AB line and EF line in Figure 4a and 4b, respectively. The vertical cross sections of reflectivity factor (Figure 5a and 5b) show that rain cell A is shallow and weak precipitation, while rain cell B is deep convective precipitation. The strong echo (greater than 38 dBZ) of rain cell B displays higher, near to 16 km. The visible reflectivity (Figure 5c and 5d) from the cloud tops of the two rain cells varies between 0.4 and 0.8, and the reflectivity of the strong echo region in rain cell B is higher (greater than 0.6). The near infrared reflectivity (Figure 5c and 5d) varies from 0.1 to 0.4, which means there are a lot of ice particles inside cloud for the two rain cells. The infrared brightness temperature at VIRS channel 3.7 μm (Figure 5e and 5f) shows higher in rain cell A, relatively lower in rain cell B, which indicates the difference between the two rain cells. At VIRS channel 10.8 μm and 12.0 μm, rain cell A has uniform brightness temperature, one of the characteristics of cloud top for stratiform precipitation system, while rain cell B appears the characteristics of deep convective cloud top, high cloud top with low brightness temperature. For the four horizontal polarization channels of TMI (Figure 5i and 5j), the microwave brightness temperature of rain cell A is uniformly distributed, and the brightness temperature of each channel has little difference. In rain cell B, the brightness temperature at low-frequency channel, 10 GHz and 19 GHz, is also evenly distributed, and the brightness temperature at the two channels is higher than that in rain cell A, but the brightness temperature at channel 37 GHz and 85 GHz changes significantly. Corresponding to the strong echo region in Figure 5b, the brightness temperature of the two channels is low, indicating that there are more ice particles inside cloud in strong echo region of rain cell B. The above indicates that the established new data can be used to analyze the corresponding spectral and microwave characteristics of precipitating clouds.

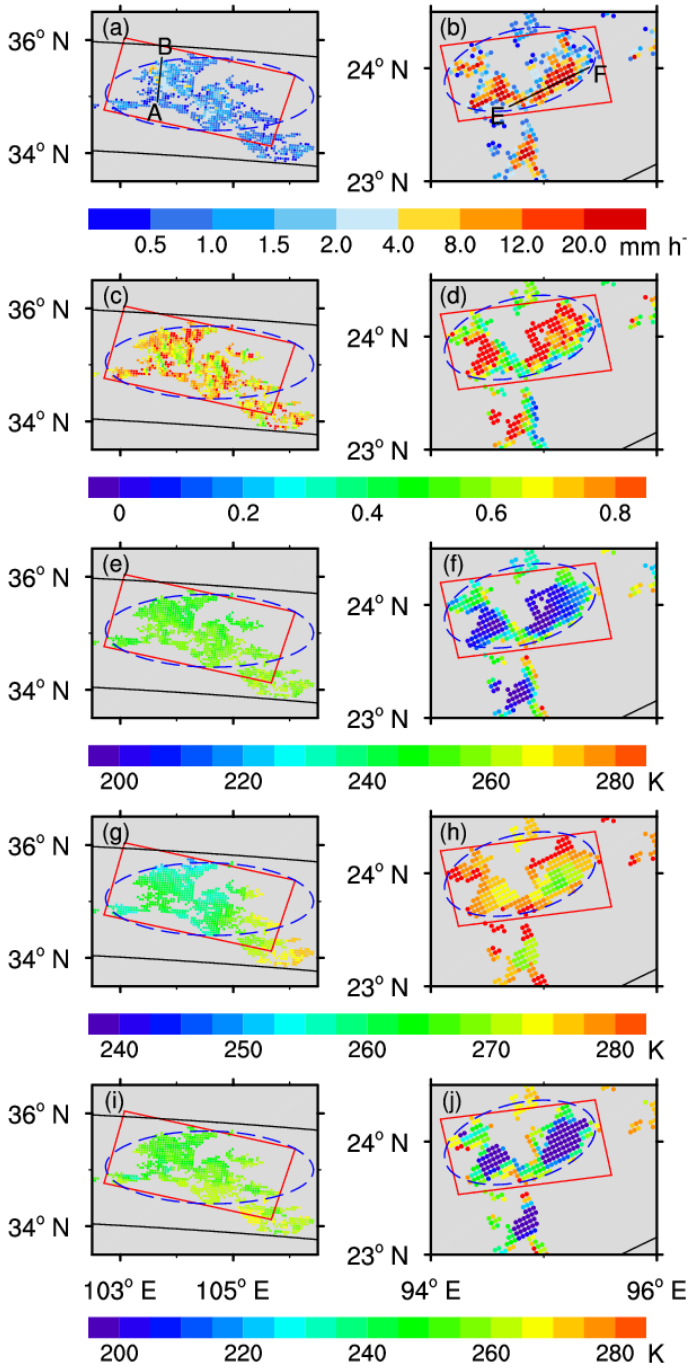

Figure 4. The distributions of near-surface rain rate (a and b), reflectivity at channel 0.63 μm (c and d), brightness temperature at far-infrared channel 10.8 μm (e and f), brightness temperature at horizontal channel 19 GHz (g and h) and at 85 GHz (i and j) for the two cases based on the merged data.

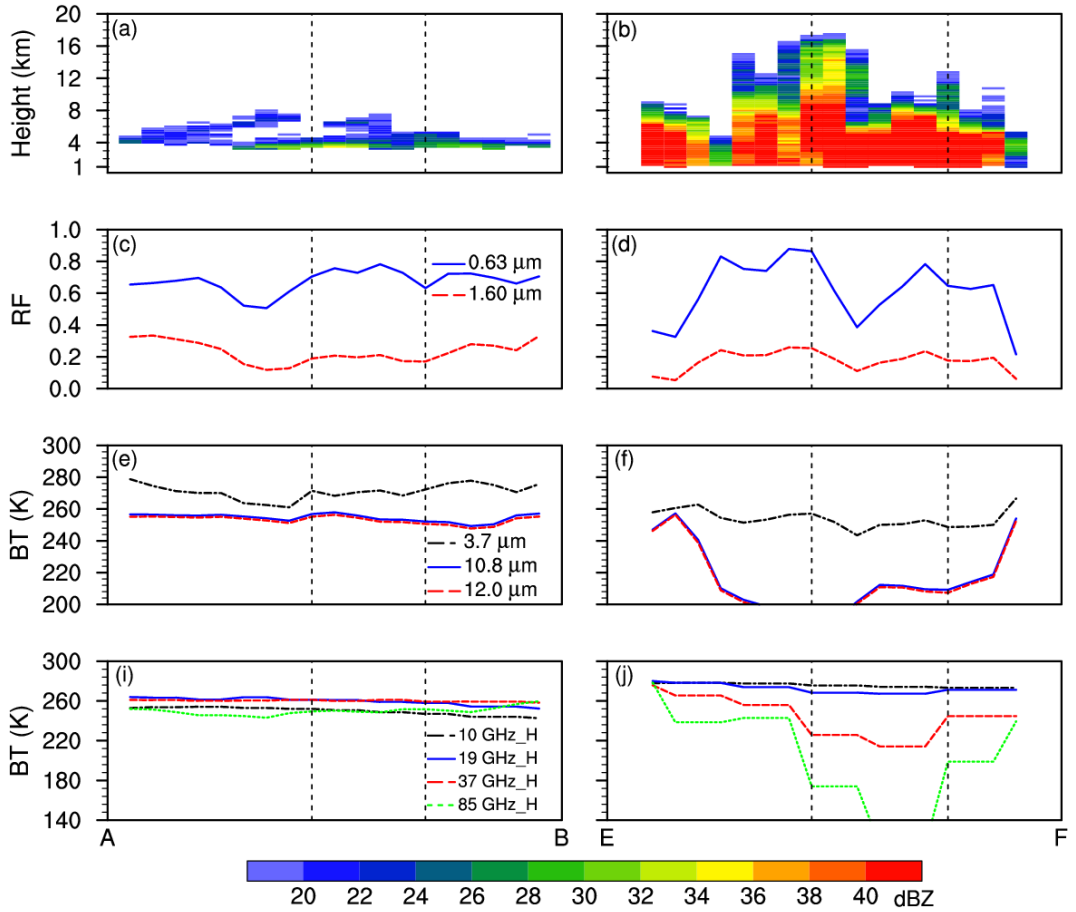

Figure 5. The vertical cross sections of reflectivity factor (a and b), reflectivity at VIRS channel 0.63 μm and 1.60 μm (c and d), infrared brightness temperature at VIRS channel 3.7 μm, 10.8 μm and 12.0 μm (e and f), microwave brightness temperature at TMI horizontal channel 10 GHz, 19 GHz, 37 GHz and 85 GHz along AB line and EF line as shown in Figure 4a and 4b.

6 Data availability

The rain cell dataset based on identification methods of MBR and BFE together with defined geometric and physical parameters to describe rain cell characteristics used in this study is accessible at https://doi.org/10.5281/zenodo.13118878.

7 Conclusions

In order to study the characteristics of geometric and physical parameters of rain cell, the basic unit in natural precipitation system, this study was inspired by earlier studies and made full use of the advantages of TRMM PR, VIRS and TMI observations, i.e. the precipitation profile of PR reflecting precipitation structure, the visible and infrared signals of VIRS representing cloud top information, and the microwave signals of TMI reflecting hydrometeors in cloud columns. By matching and merging these data at PR

pixels, the minimum bounding rectangle (MBR) method and the best fit ellipse (BFE) method were used to identify rain cell within PR scanning width, and the geometric and physical parameters of the rain cell were defined, thus a new rain cell data was established.

In this study, the geometric parameters (length, width, height and so on) and physical parameters (rain rate, visible reflectivity and thermal infrared brightness temperature from cloud top, and microwave brightness temperature from cloud column) of the two rain cells (weak rain cell and strong rain cell) identified by MBR method and BFE method are calculated. The results show that the weak rain cell shows stratiform precipitation with small rain rate, while the strong rain cell exhibits convective precipitation with deep in vertical direction and also has low thermal infrared bright temperature in cloud top. All these indicate that the both MBR method and BFE method for rain cell identification, and the defined rain cell parameters are reasonable and intuitive.

It must be noted that the difference between MBR method and BFE method is only in the horizontal geometric parameters of the rain cell, and the difference is not large, such as the slight difference in length and width of the rain cell, but the vertical geometric parameters of the rain cell are not affected. The physical parameters of the rain cell are not affected by the identification method.

The new rain cell data in this study can be used to study the characteristics of rain cell geometric and physical parameters. Although a lot of achievements have been made in this aspect, systematic and in-depth analysis is still needed, such as the regional differences of these parameters and the characteristics of climate change. It can also be used to analyze the relationship between the physical and geometric parameters of rain cell, which also have regional differences. The effective radius of cloud particles, optical thickness, liquid water path and other parameters in rain cell can be obtained by combining retrieval algorithms of visible and near infrared reflectivity, which can analyze the characteristics of cloud physical parameters of rain cell. These parameters such as cloud water and ice water in column, cloud temperature and rain rate in rain cell can also be obtained by using microwave brightness temperature retrieval algorithms, and the relationship among these parameters can be analyzed. It is believed that the previously mentioned studies will produce results shortly.

Author contribution. ZW and YF prepared the data in the standardized format. ZW uploaded the data in the data repository and prepared the manuscript with contribution from YF. All the authors discussed

the concepts and edited the manuscript.

Competing interests. The authors declare that they have no conflict of interest.

Acknowledgements. We would like to acknowledge the National Aeronautics and Space Administration (NASA) for providing TRMM PR, VIRS and TMI datasets.

Financial support. This research has been supported by the National Natural Science Foundation of China (grant nos. 42230612 and 42275140) and The Second Tibetan Plateau Scientific Expedition and Research (STEP) program (grant no. 2019QZKK0104)

References

Austin, P. M. and Houze, R. A.: Analysis of the structure of precipitation patterns in New England, J. Appl. Meteorol., 11, 926–935, https://doi.org/10.1175/1520-0450(1972)011<0926:Aotsop>2.0.Co;2, 1972.

Awaka, J.: A three-dimensional rain cell model for the study of interference due to hydrometeor scattering, J. Commun. Res. Lab., 36, 13–44, 1989.

Awaka, J., Iguchi, T., Kumagai, H., and Okamoto, K.: Rain type classification algorithm for TRMM precipitation radar, IEEE International Geoscience and Remote Sensing Symposium Proceedings. Remote Sensing – A Scientific Vision for Sustainable Development, Singapore, 3–8 August 1997, https://doi.org/10.1109/IGARSS.1997.608993, 1997.

Begum, S. and Otung, I. E.: Rain cell size distribution inferred from rain gauge and radar data in the UK, Radio. Sci., 44, RS2015, https://doi.org/10.1029/2008RS003984, 2009.

Cai, H. K., Mao, Y. Q., Zhu, X. H., Fu, Y. F., and Zhou, R. J.: Comparison of the minimum bounding rectangle and minimum circumscribed ellipse of rain cells from TRMM, Adv. Atmos. Sci., 41, 484–499, https://doi.org/10.1007/s00376-023-2281-9, 2024.

Capsoni, C., Fedi, F., Magistroni, C., Paraboni, A., and Pawlina, A.: Data and theory for a new model of the horizontal structure of rain cells for propagation applications, Radio. Sci., 22, 395–404,

https://doi.org/10.1029/RS022i003p00395, 1987.

Chen, Y. L., Zhang, A. Q., Fu, Y. F., Chen, S. M., and Li, W. B.: Morphological characteristics of precipitation areas over the Tibetan Plateau measured by TRMM PR, Adv. Atmos. Sci., 38(4), 677–689, https://doi.org/10.1007/s00376-020-0233-1, 2021.

Han, Q., Rossow, W. B., and Lacis, A. A.: Near-global survey of effective droplet radii in liquid water clouds using ISCCP data, J. Climate, 7, 465–497, https://doi.org/10.1175/1520-0442(1994)007<0465:NGSOED>2.0.CO;2, 1994.

Feral, L., Mesnard, F., Sauvageot, H., Castanets, L., and Lemorton, J.: Rain cells shape and orientation distribution in south-west of France, Phys. Chem. Earth B: Hydrol. Oceans Atmos., 25, 1073–1078, https://doi.org/10.1016/s1464-1909(00)00155-6, 2000.

Fu, Y. F.: Cloud parameyers retrieved by the bispectral reflectance algorithm and associated applications, J. Meteorol. Res-Prc., 28, 965–982, https://doi.org/10.1007/s13351-014-3292-3, 2014 (in Chinese).

Fu, Y. F.: Research progress on retrieval algorithms of cloud liquid water over ocean based on remote sensing by satellite-borne passive microwave instruments, Torrential Rain and Disasters, 40, 217–230, https://doi.org/10.3969/j.issn.1004-9045.2021.03.001, 2021 (in Chinese).

Fu, Y. F., Chen, Y., Zhang, X., Wang, Y., Li, R., Liu, Q., Zhong, L., Zhang, Q., and Zhang, A.: Fundamental characteristics of tropical rain cell structures as measured by TRMM PR, J. Meteorol. Res-Prc., 34, 1129–1150, https://doi.org/10.1007/s13351-020-0035-5, 2020.

Fu, Y. F. and Liu, G. S.: The variability of tropical precipitation profiles and its impact on microwave brightness temperatures as inferred from TRMM data, J. Appl. Meteorol., 40, 2130–2143, https://doi.org/10.1175/1520-0450(2001)040<2130:Tvotpp>2.0.Co;2, 2001.

Fu, Y. F., Liu, P., Liu, Q., Ma, M., Sun, L., and Wang, Y.: Climatological Characteristics of VIRS Channels for Precipitating Cloud in Summer Over the Tropics and Subtropics, J. Atmos. Environ. Optics., 6, 129–140, https://doi.org/10.3969/j.issn.1673- 6141.2011.02.009, 2011 (in Chinese).

Gagin, A., Rosenfeld, D., Woodley, W. L., and Lopez, R. E.: 1986: Results of seeding for dynamic effects on rain-cell properties in FACE-2, J. Appl. Meteor. Climatol., 25, 3–13, https://doi.org/10.1175/1520-0450(1986)025<0003:ROSFDE>2.0.CO;2, 1986.

Goldhirsh, J. and Musiani, B.: Rain cell size statistics derived from radar observations at Wallops Island, Virginia, IEEE T. Geosci. Remote. Sens., GE-24, 947–954, https://doi.org/10.1109/TGRS.1986.289711,

1986.

Grody, N. C.: Remote sensing of atmospheric water content from satellites using microwave radiometry, IEEE T. Antenn. Propag., 24, 155–162, https://doi.org/10.1109/TAP.1976.1141324, 1976.

Grody, N. C., Grubel, A., and Shen, W. C.: Atmospheric water content over the tropical Pacific derived from the Nimbus-6 scanning microwave spectrometer, J. Appl. Meteor., 19, 986–996, https://doi.org/10.1175/1520-0450(1980)019<0986:AWCOTT>2.0.CO;2, 1980.

He, H. Z., Cheng, M. H., and Zhou, F. X.: 3D structure of rain and cloud hydrometeors for Typhoon Kujira (0302), Chinese J. Atmos. Sci., 30, 491–503, https://doi.org/ 10.3878/j.issn.1006-9895.2006.03.12, 2006 (in Chinese).

Houze, R. A.: Structures of atmospheric precipitation systems: A global survey, Radio. Sci., 16, 671–689, https://doi.org/10.1029/RS016i005p00671, 1981.

Houze, R. A.: Stratiform Precipitation in Regions of Convection: A Meteorological Paradox?, B. Am. Meteorol. Soc., 78, 2179–2196, https://doi.org/10.1175/1520- 0477(1997)078<2179:SPIROC>2.0.CO;2, 1997.

Konrad, T. G.: Statistical models of summer rainshowers derived from fine-scale radar observations, J. Appl. Meteorol., 17, 171–188, https://doi.org/10.1175/1520-0450(1978)017<0171:SMOSRD>2.0.Co;2, 1978.

Kozu, T., Kawanishi, T., Kuroiwa, H., Oikawa, M., Kumagai, H., Okamoto, K., Okumura, M., Nakatsuka, H., and Nishikawa, K.: Development of precipitation radar onboard the Tropical Rainfall Measuring Mission (TRMM) satellite., IEEE T. Geosci. Remote. Sens., 39, 102–116, https://doi.org/10.1109/36.898669, 2001.

Kummerow, C., Barnes, W., Kozu, T., Shiue, J., and Simpson, J.: The Tropical Rainfall Measuring Mission (TRMM) Sensor Package, J. Atmos. Ocean. Tech., 15, 809–817, https://doi.org/10.1175/1520-0426(1998)015<0809:TTRMMT>2.0.Co;2, 1998.

Kummerow, C., Simpson, J., Thiele, O., Barnes, W., Chang, A. T. C., Stocker, E., Adler, R. F., Hou, A., Kakar, R., Wentz, F., Ashcroft, P., Kozu, T., Hong, Y., Okamoto, K., Iguchi, T., Kuroiwa, H., Im, E., Haddad, Z., Huffman, G., Ferrier, B., Olson, W. S., Zipser, E., Smith, E. A., Wilheit, T. T., North, G., Krishnamurti, T., and Nakamura, K.: The Status of the Tropical Rainfall Measuring Mission (TRMM) after two years in orbit, J. Appl. Meteorol. Climatol., 39, 1965–1982, https://doi.org/10.1175/1520-

0450(2001)040<1965:Tsottr>2.0.Co;2, 2000.

Lau, K. M. and Wu, H. T.: Characteristics of precipitation, cloud, and latent heating associated with the Madden-Julian oscillation, J. Climate, 23, 504–518, https://doi.org/10.1175/2009jcli2920.1, 2010.

Li, R. and Fu, Y. F.: Tropical precipitation estimated by GPCP and TRMM PR observations, Adv. Atmos. Sci., 22, 852–864, https://doi.org/10.1007/BF02918685, 2005.

Liu, C. T., Zipser, E. J., and Nesbitt, S. W.: Global distribution of tropical deep convection: different perspectives from TRMM infrared and radar data, J. Climate, 20, 489–503, https://doi.org/10.1175/JCLI4023.1, 2007.

Liu, C. T., Zipser, E. J., Cecil, D. J., Nesbitt, S. W., and Sherwood, S.: A cloud and precipitation feature database from nine years of TRMM observations, J. Appl. Meteorol. Climatol., 47, 2712–2728, https://doi.org/10.1175/2008jamc1890.1, 2008.

Liu, C. T. and Zipser, E. J.: Regional variation of morphology of organized convection in the tropics and subtropics, J. Geophys. Res.-Atmos., 118, 453–466, https://doi.org/10.1029/2012JD018409, 2013.

Liu, G. S. and Curry, J. A.: Determination of characteristic features of cloud liquid water from satellite microwave measurements, J. Geophys. Res., 98, 5069–5092, https://doi.org/10.1029/92JD02888, 1993.

Liu, G. S. and Fu, Y. F.: The characteristics of tropical precipitation profiles as inferred from satellite radar measurements, J. Meteor. Soc. Japan, 79, 131–143, https://doi.org/10.2151/jmsj.79.131, 2001.

Liu, Q. and Fu, Y. F.: Comparison of radiative signals between precipitating and non-precipitating clouds in frontal and typhoon domains over East Asia, Atmos. Res., 96, 436–446, https://doi.org/10.1016/j.atmosres.2010.02.003, 2010.

Nakajima, T. and King, M. D.: Determination of the optical thickness and effective particle radius of clouds from reflected solar radiation measurements. Part I: Theory, J. Atmos. Sci., 47, 1878–1893, https://doi.org/10.1175/1520-0469(1990)047<1878:DOTOTA>2.0.CO;2, 1990.

Nesbitt, S. W., Cifelli, R., and Rutledge, S. A.: Storm morphology and rainfall characteristics of TRMM precipitation features, Mon. Wea. Rev., 134, 2702–2721, https://doi.org/10.1175/MWR3200.1, 2006.

Nesbitt, S. W., Zipser, E. J., and Cecil, D. J.: A census of precipitation features in the tropics using TRMM: Radar, ice scattering, and lightning observations, J. Climate, 13, 4087–4106, https://doi.org/10.1175/1520-0442(2000)013<4087:ACOPFI>2.0.Co;2, 2000.

Ni, X., Liu, C., Zhang, Q., and Cecil, D. J.: Properties of hail storms over China and the United States

446 from the Tropical Rainfall Measuring Mission, J. Geophys. Res.-Atmos., 121, 12031–12044,
447 https://doi.org/10.1002/2016JD025600, 2016.
448 Oki, T. and Kanae, S.: Global hydrological cycles and world water resources, Science, 313, 1068–1072,
449 https://doi.org/10.1126/science.1128845, 2006.
450 Petty, G.W.: Physical retrievals of over-ocean rain rate from multichannel microwave imagery. Part I:
451 Theoretical characteristics of normalized polarization and scattering indices, Meteorl. Atmos. Phys., 54,
452 79–99, https://doi.org/10.1007/BF01030053, 1994a.
453 Petty, G.W.: Physical retrievals of over-ocean rain rate from multichannel microwave imagery. Part II:
454 Algorithm implementation, Meteorl. Atmos. Phys., 54, 101–121, https://doi.org/10.1007/BF01030054,
455 1994b.
456 Rossow, W. B. and Garder, L. C.: Cloud detection using satellite measurements of infrared and visible
457 radiances for ISCCP, J. Climate, 6, 2341–2369, https://doi.org/10.1175/1520-
458 0442(1993)006<2341:CDUSMO>2.0.CO;2. 1993.
459 Rossow, W. B. and Schiffer, R. A.: Advances in understanding clouds from ISCCP, Bull. Amer. Meteor.
460 Soc., 80, 2261–2288, https://doi.org/10.1175/1520-0477(1999)080<2261:AIUCFI>2.0.CO;2, 1999.
461 Sauvageot, H., Mesnard, F., and Tenório, R. S.: The relation between the area-average rain rate and the
462 rain cell size distribution parameters, J. Atmos. Sci., 56, 57–70, https://doi.org/10.1175/1520-
463 0469(1999)056<0057:TRBTAA>2.0.Co;2, 1999.
464 Schumacher, C. and Houze, R. A.: The TRMM precipitation radar's view of shallow, isolated rain, J.
465 Appl. Meteorol., 42, 1519–1524, https://doi.org/10.1175/1520-
466 0450(2003)042<1519:TTPRVO>2.0.CO;2, 2003.
467 Simpson, J., Kummerow, C., Tao, W.-K., and Adler, R. F.: On the Tropical Rainfall Measuring Mission
468 (TRMM), Meteorol. Atmos. Phys., 60, 19–36, https://doi.org/10.1007/BF01029783,1996.
469 Sun, L. L. and Fu, Y. F.: A new merged dataset for analyzing clouds, precipitation and atmospheric
470 parameters based on ERA5 reanalysis data and the measurements of the Tropical Rainfall Measuring
471 Mission (TRMM) precipitation radar and visible and infrared scanner, Earth Syst. Sci. Data, 13, 2293–
472 2306, https://doi.org/10.5194/essd-13-2293-2021, 2021.
473 Viltard, N., Kummerow, C., Olson, W. S., and Hong, Y.: Combined use of the radar and radiometer of
474 TRMM to estimate the influence of drop size distribution on rain retrievals, J. Appl. Meteorol., 39, 2103–

2114, https://doi.org/10.1175/1520-0450(2001)040<2103:Cuotra>2.0.Co;2, 2000.

Wang, Y., Fu, Y. F., Liu, G. S., Liu, Q., and Sun, L.: A new water vapor algorithm for TRMM Microwave Imager (TMI) measurements based on a log linear relationship, J. Geophys. Res., 114, D21304, https://doi.org/10.1029/2008JD011057, 2009.

Wu, Z. H. and Fu, Y. F.: A new dataset of rain cell generated from observations of the Tropical Rainfall Measuring Mission (TRMM) precipitation radar and visible and infrared scanner and microwave imager [Data set], Zenodo, https://doi.org/10.5281/zenodo.13118878, 2024.

Yokoyama, C., Zipser, E. J., and Liu, C.: TRMM-Observed shallow versus deep convection in the eastern pacific related to large-scale circulations in reanalysis datasets, J. Climate, 27, 5575–5592, https://doi.org/10.1175/JCLI-D-13-00315.1, 2014.

Yuter, S. E. and Houze, R. A.: Three-Dimensional kinematic and microphysical evolution of florida cumulonimbus. Part II: frequency distributions of vertical velocity, reflectivity, and differential reflectivity, Mon. Weather Rev., 123, 1941–1963, https://doi.org/10.1175/1520-0493(1995)123<1941:Tdkame>2.0.Co;2, 1995.

Zhou, Y., Lau, W. K. M., and Liu, C. T.: Rain characteristics and large-scale environments of precipitation objects with extreme rain volumes from TRMM observations, J. Geophys. Res.-Atmos., 118, 9673–9689, https://doi.org/10.1002/jgrd.50776, 2013.

Zipser, E. J. and Lutz, K. R.: The vertical profile of radar reflectivity of convective cells: A strong indicator of storm intensity and lightning probability?, Mon. Weather Rev., 122, 1751–1759, https://doi.org/10.1175/1520-0493(1994)122<1751:Tvporr>2.0.Co;2, 1994.